



HAL
open science

LIBS for Characterizing Nanomaterials

Christophe Dutouquet, Jörg Hermann

► **To cite this version:**

Christophe Dutouquet, Jörg Hermann. LIBS for Characterizing Nanomaterials. Nandakumar Kalarikkal; Rodolphe Antoine; Sabu Thomas; Padiyakkuth Nideesh. Laser-based Techniques for Nanomaterials: Processing to Characterization, Royal Society of Chemistry, pp.235-261, 2024, Optical, Electronic and Magnetic Materials, 978-1-83767-128-1. 10.1039/9781837673513-00235 . hal-04844078

HAL Id: hal-04844078

<https://hal.science/hal-04844078v1>

Submitted on 17 Dec 2024

HAL is a multi-disciplinary open access archive for the deposit and dissemination of scientific research documents, whether they are published or not. The documents may come from teaching and research institutions in France or abroad, or from public or private research centers.

L'archive ouverte pluridisciplinaire **HAL**, est destinée au dépôt et à la diffusion de documents scientifiques de niveau recherche, publiés ou non, émanant des établissements d'enseignement et de recherche français ou étrangers, des laboratoires publics ou privés.

Chapter 10

LIBS for characterizing nanomaterials

Christophe Dutouquet^{a*} and Jörg Hermann^b

^a INERIS (French National Institute for Industrial Environment and Risks), Parc Technologique Alata BP 2 F-60550 Verneuil-en-Halatte, France,

^b Aix-Marseille University, CNRS, LP3, 13288 Marseille, France

*corresponding email address: christophe.dutouquet@ineris.fr

ABSTRACT

Nano-objects, their aggregates and their agglomerates are currently used in the industry to manufacture materials with advanced functionalities. Their use requires new tools in diverse fields such as workplace surveillance or process control. Indeed, little is known yet concerning the adverse effects these objects may have on human health and the environment. There is therefore a need to design tools allowing their in-situ real-time detection and characterization during the manufacturing process. In this context, LIBS is seen as a potential candidate for these applications. It was applied to the detection of carbon nanotube balls for workplace surveillance and to the compositional analysis of SiC_x nanopowders for process control. For this latter issue, the so-called calibration-free LIBS analysis based on modelling of the laser-induced plasma emission spectrum proved to be a real asset. A new method for particle analysis has been tested. It consists in trapping particles in a radio-frequency plasma discharge for LIBS analyses. Such an approach presents several advantages further discussed in this chapter.

10.1 Introduction

Nanotechnology is often said to be the industry of the 21st century. Nanostructured materials are expected to lead to the emergence of new products with enhanced features and functionalities. Their manufacturing often requires the use of nanostructured particles with different sizes, shapes and chemical compositions referred to as Nano Objects, their Aggregates, and their Agglomerates (NOAA). These are the basic building blocks used to design nanostructured materials. Carbon nanotubes (CNT) are often presented as a future superstar in the field of nanotechnology. Their mechanical and electrical properties were demonstrated to be remarkable in comparison with other materials. They are about 100 times more resistant than steel while being six times lighter. They are envisaged to reinforce polymer materials or to reduce wear, as for instance in case of tyres. They could play an important role in the field of information technology owing to their excellent electric conductivity. Silicon carbide nanopowders are another telling example. Of importance in the nuclear industry, silicon carbide is a promising material for high temperature applications. Its properties happen to be enhanced when prepared using SiC_x in nanostructured form. These are a few examples of the potentialities offered by nanostructured materials. The detection of carbon nanotubes balls and of SiC_x nanopowders using Laser-Induced Breakdown Spectroscopy (LIBS) will be presented below.

The advent of these new objects raises the question of the development of an adapted metrology for their characterization in various contexts. Two examples of need may be underlined. First, little is known yet about the risks related to nano-objects in terms of impact on human health and the environment. There is therefore a need to detect and characterize these particles for instance in the workplace. Second, production processes require tools for on-line characterization of the final product. Thus, adequate instruments enabling on-site, on-line and even real-time monitoring of size-, number density, and chemical composition of the particles must be designed to meet the aforementioned needs. LIBS^{1,2} was deemed as a promising technique to deal with such issue.

In this chapter, we will first present the application of LIBS to workplace surveillance. Then we will examine the use of LIBS for process control when analysing SiC_x nanopowders. After that, the advantages brought by plasma modelling for process control will be discussed. In the end, the possibility to analyse NOAA coupling LIBS with a radio frequency plasma cell will be presented³.

10.2 What is Laser-Induced Breakdown Spectroscopy?

LIBS^{4,5,6,7} consists in focusing a powerful laser pulse on a material (solid, liquid, gas, aerosol, nanoparticle flow) whose elemental composition is to be determined. The strong heating of the sample at the focusing spot leads to the ignition of a hot and luminous transient ionized gas called plasma. The plasma emission spectrum contains the signature of all the chemical elements composing the sample material as shown in figure 10.1. The emission spectrum is recorded with the aid of a spectrometer equipped with a detector. The abundance of each element can be deduced from the intensity of the corresponding spectral lines. Properly calibrated, the intensity is proportional to the detected amount of matter and may be, for

instance, expressed in $\mu\text{g m}^{-3}$ when analysing nanoobjects, their aggregates, and their agglomerates in aerosol form. Aerosols may be defined as an ensemble of solid and / or liquid particles suspended in a gas with sizes ranging from a few nanometres to a few hundreds of micrometres.

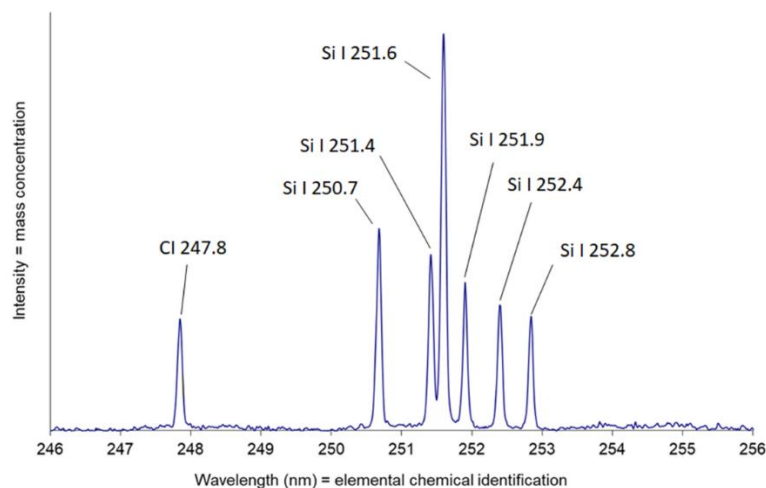


Figure 10.1. LIBS spectrum of SiC_x nanopowders suspended in argon gas.

LIBS combines several advantages of great interest for industrial applications. Detection of all the elements is possible at various pressure conditions. In addition, samples do not need preliminary preparation making LIBS eligible for on-line monitoring. Being all optical, the technique is non-intrusive, requires only optical access to the sample, and enables thus in-situ measurements. LIBS is potentially fast and suitable for real-time monitoring, its speed depending on the number of laser shots required to obtain reliable results. Remote or stand-off analyses are possible. The aforementioned features do make LIBS a promising analytical chemistry method intended to be operated on industrial sites. Current elemental analysis techniques require time-consuming procedures involving several steps. Skilled personnel are sent to the sites where samples are to be picked up. Back to the laboratory, these are prepared prior to the analysis itself. The LIBS systems dedicated to aerosol analysis are intended to be operated on-site, in fully automated operation, without manual intervention except for maintenance. The LIBS technique is therefore promising for many applications.

In LIBS experiments, two important parameters, the time delay and the integration time, are worth presenting. Indeed, the laser-induced plasma has a transient nature. It is characterized by a fast time-evolution and mostly by spatially non-uniform distribution of temperature and densities. The plasma lifetime is of about a few tens of microseconds and its dimensions of around a few millimetres at full expansion. This has a consequence on the detection. In order to get the best signal-to-noise ratio, LIBS spectra are mostly recorded with gated detectors of temporal resolution in the nanosecond range. This is the consequence of the properties of the laser-induced plasma. During the early times of its ignition, the lines of analytical interest are not visible, masked by a strong continuum radiation. Thus, spectra are recorded with a precise delay and integration time or gate width. The delay represents the duration elapsed between the laser pulse and the detector gate. The integration time refers to the duration of the spectrum recording. These two parameters are worth presenting as they will always be found when reading LIBS literature.

10.3 LIBS applied to the detection of particles

The particle analysis via LIBS is illustrated in figure 10.2 for (a) high and (b) low particle concentrations. In the first case (a) observed in most LIBS applications, the recording is typically operated by accumulating the signal over several laser shots to obtain satisfying signal to background ratio. This approach is for example applied to analyse a dense flow of nanopowders in process control (see SiC_x detection in section 10.5.4).

In the opposite case (b), when the particle concentration is low, say a few hundreds of $\mu\text{g m}^{-3}$ with micrometric-sized particles, the simple signal accumulation no longer ensures the optimisation of the signal-to-noise ratio. When the probability of the presence of the particle within the plasma is below unity, conditional analysis may be applied to improve the sensitivity^{8,9,10}. It consists in accumulating only spectra that contain the signature of the detected particle, discarding thus the blank spectra recorded when no particle is in the laser-produced plasma.

This recording mode was for example selected for measurements of micrometric-sized CNT balls¹¹. It should be noted that for micrometric-sized particles, single particle analysis is made possible, and this capacity was utilized for CNT ball detection.

Hahn and co-workers^{8,9,10} demonstrated that particles are sampled by the laser-induced plasma, and not directly by the interaction with the laser beam. As the result of fast plasma expansion, the plasma volume is much larger than the focal volume of the laser beam, and the probability to observe a particle in the plasma is therefore much larger than the probability to find the particle in the focal volume. The transient nature of the laser-induced plasma and the discrete nature of particles make LIBS detection under these conditions a highly stochastic process.

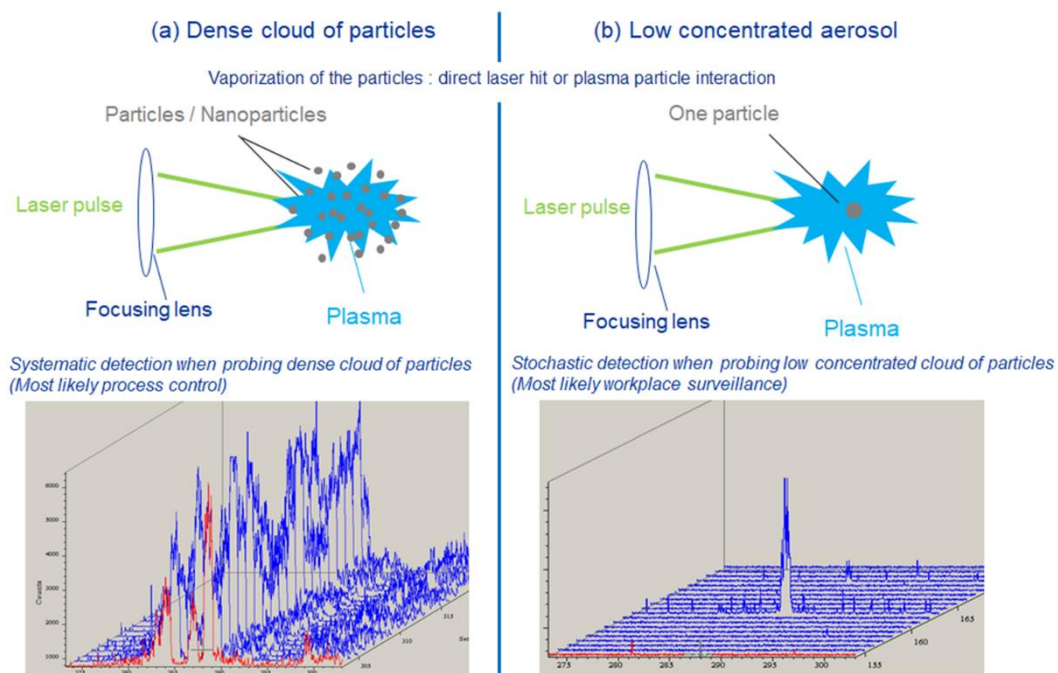


Figure 10.2. LIBS spectra recorded for consecutive laser pulses in the cases of (a) dense and (b) low-concentrated clouds of particles

Hahn and co-workers^{8,9} define the Particle Sampling Rate (PSR) representing the ratio of the number of successful particle detections over the total number of applied laser pulses. The knowledge of the particle sampling rate makes the evaluation of the sampling volume possible.

The probability to detect k particles in the plasma produced by a single laser pulse calculated according to Poisson's law is

$$P_k = \frac{\mu^k}{k!} \exp(-\mu), \quad (10.1)$$

where μ is the average number of particles per plasma volume given by

$$\mu = N V_S. \quad (10.2)$$

Here, N is the number density of particles and V_S is the plasma sampling volume. The particle sampling rate being the probability to sample at least one particle is given by

$$PSR = 100 \times (1 - P_0) = 100 \times (1 - \exp(-\mu)), \quad (10.3)$$

where P_0 is the probability of zero particle sampling.

Combining equations (10.2) and (10.3), the sampling volume can be calculated as

$$V_S = -\frac{\ln(1 - PSR/100)}{N}. \quad (10.4)$$

Thus, when the PSR is low ($\leq 10\%$), equation (10.4) simplifies to

$$V_S = \frac{PSR}{100 \times N}. \quad (10.5)$$

The sampling volume can thus be obtained from equation (10.5) when the particle sampling rate is measured in the course of the experiments and the particle concentration is known. Hahn and co-workers demonstrated with their experiments that the Poisson's law is appropriate to model the particle sampling rate¹².

10.4 LIBS detection in the workplace: example of CNT balls

LIBS has the ability to detect CNT balls suspended in the air. To prove this capability, experiments were performed by combining a LIBS system with an aspiration Transmission Electron Microscope (TEM) sampler. Three handling scenarios were realised in a high safety room that enabled the simulation of realistic operations¹¹.

10.4.1. CNT manufacturing

There are many ways to manufacture CNT balls. The fluidized bed catalytic chemical vapor deposition technique (CCVD) is one of them. The basic principle of such a technique can be briefly described as follows¹³. A gas mixture containing a hydrocarbon gas (e.g. ethylene) and a carrier gas flows upwards through a vertical reactor enclosed within a furnace. Alumina particles supporting iron nanoparticles playing the role of catalysts in CNT growth are then

fluidized by the aforementioned gas flow. Ethylene bonds are broken when entering into contact with nanometric particles of iron at temperatures ranging from 700 to 1200°C. Free carbon atoms are then deposited on the metallic nanoparticles thereby leading to CNT growth. The final product is a powder of micrometric-sized balls with an average size of about a few hundreds of micrometres containing intertwined carbon nanotubes (Multi wall CNTs or MWCNTs implying the presence of carbon) as well as Fe and Al originating from catalyst and catalyst support, respectively. The CNT balls are presented in figure 10.3. Thus, the CNT balls are made of carbon, iron and aluminium that are elements being detectable using LIBS. They are nanostructured particles with sizes ranging from a few micrometres to several tens of micrometres.

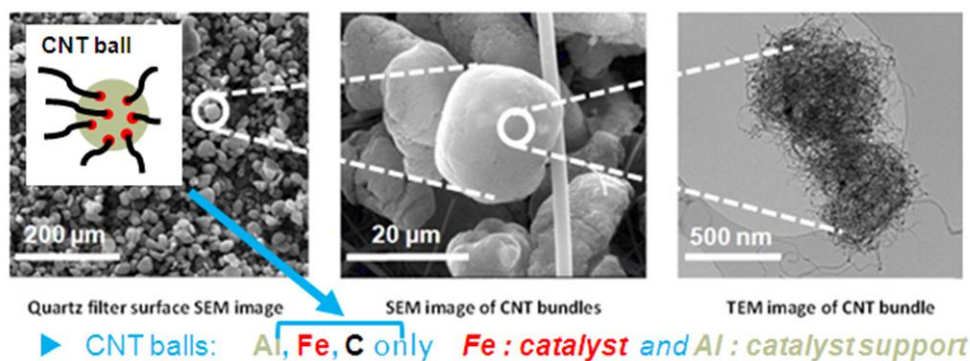


Figure 10.3. Scanning electron microscope and transmission electron microscope images showing CNT balls (Adapted from Ref. 3 with permission from Spectroscopy, copyright 2015)

10. 4. 2. Handling scenarios

Handling experiments were carried out by an operator wearing a chemical protective suit specially fitted for hazardous environment in a high safety room dedicated to scientific experiments. High-efficiency ventilation enables the extraction of potentially contaminated ambient air through a high efficiency filter. This installation provided the user with real handling conditions thereby avoiding raising the question of how realistic particle stirring was. The instruments were installed in a room next to the laboratory where the CNT powder was handled. The sampling lines allowing particle detection were passed through holes drilled in a plastic window shared by both rooms. Room clean-up after the experiments was ensured by flushing out ground and walls with pressurized water. Three handling scenarios of 20 to 30-minutes duration were retained. The first two involved a rather improbable way of handling powders, much closer to accidental tipping than to normal working conditions. These were chosen to start experiments with a high particle density to facilitate instrument adjustments and to ensure preliminary detection. The first scenario consisted of continuously pouring one full jar of CNT powders into another while ventilation had been shut off. The second scenario was identical to the previous, except of the ventilation that this time was turned on. The last scenario, quite close to routine operations, consisted of shovelling up a small amount of CNT powder from a bucket and to pour it into a jar for weighing prior to packaging, while the ventilation was running.

10. 4. 3. LIBS & TEM sampler experimental setups

A scheme of the experimental setup for CNT ball detection is presented in figure 10.4. Laser pulses of 5 ns duration, 120 mJ energy, and 20 Hz repetition rate were generated by a Q-switched Nd:YAG laser ($\lambda = 1064$ nm) and focused inside the cell using a fused silica plano-convex lens of 35 mm focal length. Before focusing, the laser beam was expanded to three times its original diameter (6 mm).

This resulted in the igniting of a laser-induced plasma right in the particle flow. The outlet end of the LIBS cell was connected to a pump operating at 16 l min^{-1} and ensuring a constant flowrate through the cell. The fraction of the laser beam not absorbed by the plasma was directed toward a beam stop outside the cell passing through a quartz window being positioned opposite the focusing lens. A third quartz window, orientated perpendicularly to the other two, was used to collect the light emitted by the plasma for LIBS analyses purposes. The LIBS signal was collected with a 50 mm focal length lens along an axis perpendicular to the laser beam. The plasma emission was imaged onto the entrance of a $50 \mu\text{m}$ diameter core optical fibre with a magnification of $1/3$. The fibre was linked to an Echelle spectrometer of 5×10^3 resolving power coupled to a gated detector. The spectrometer enables the recording of spectra over a large range from 200 to 1000 nm.

The aspiration TEM sampler consists of a 6-mm inner diameter hollow tube where a TEM grid holder is soldered perpendicularly to the tube section near one of its capped tips. The TEM holey grid is positioned at the bottom of the grid holder, just above a critical orifice assuring a 0.3 l min^{-1} constant flowrate. A copper seal held tight against the grid keeps it in place using a hollow screw to let the air flowing in. The grid holder is inserted in a $1/2$ " swagelock tube connected to one of the sampling lines pointing towards the high safety room. The outlet end of the sampler was connected to a pump assuring the aforementioned flow rate of 0.3 l min^{-1} . The sampler was operated without impactor letting particles of all sizes flowing in without classification. Copper holey grids of 3.02 mm diameters were utilized with this sampler.

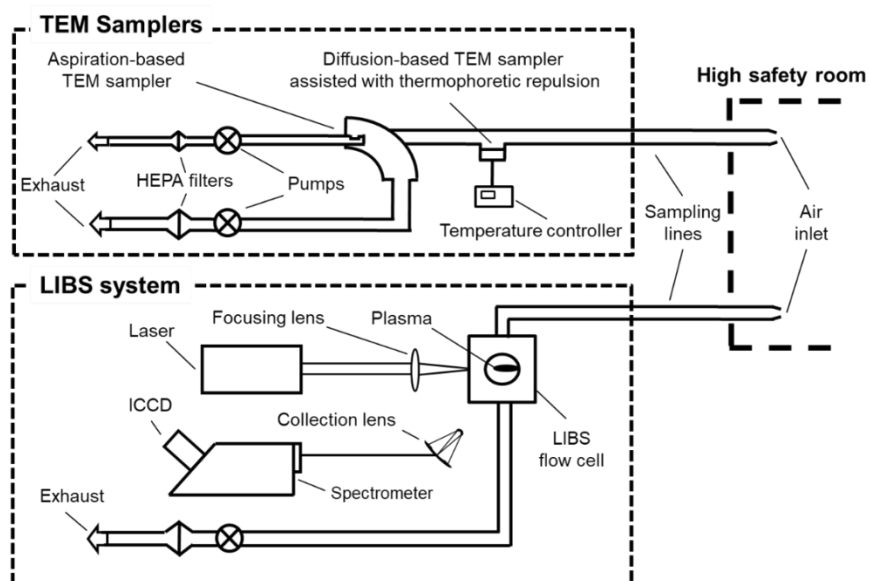


Figure 10.4. Experimental setup dedicated to CNT balls detection. Information about the operation of the diffusion-based TEM sampler assisted with thermophoretic repulsion is given in the reference. (Adapted from Ref. 11 with permission from Springer, copyright 2011)

10. 4. 4. About time delay and integration time

The temporal settings are of primary importance in LIBS experiments as the signal intensity is far from being constant over the plasma lifetime. In most cases, LIBS signal detection optimization implies resorting to detectors allowing time-resolved measurements like gated cameras. Triggering LIBS signal recording at a given delay of the detector gate after the laser pulse is required to avoid signal-to-noise lowering due to the intense continuum emission during the initial stage of plasma ignition. Moreover, the adjustment of the duration of signal acquisition by setting the gate width enables further optimization of the signal-to-noise ratio, as it avoids the noise accumulation at large delay, when the analytical signal is weak. Finally, the accumulation over a given number of laser shots reduces the standard deviation of the background signal and leads therefore to a further improvement of the signal-to-noise ratio. Compared to measurements with non-triggered and non-gated detectors, LIBS experiments with gated detectors were shown to reach significantly higher sensitivity⁴. The temporal settings can vary significantly from one LIBS experiment to another and must therefore be carefully selected. The issue of integration and delay times to be applied when analysing particles in air at atmospheric pressure was broached by Amodeo et al.¹⁴. The dependence of LIBS temporal parameters as a function of particle chemical nature and size, laser wavelength, laser energy, and background gas was presented and discussed. Taking into account these previous results, a time delay of 30 μs was chosen for aluminium and iron line detection. This delay was reduced to 5 μs for the observation of carbon line emission. The integration time was set to 80 μs in these LIBS experiments.

10. 4. 5. LIBS detection of CNT balls

Along with the LIBS experiments aiming to demonstrate the feasibility of CNT ball detection, particles emitted during the three scenarios (see section 10.4.2) were sampled on TEM grids (see figure 10.3). Their sizes varied from approximately 1 to 80 μm . CNT balls could be recognized according to their particular morphology providing a robust morphologic signature. Energy Dispersive X-ray microanalysis (EDX) analyses revealed that CNT balls were always and only composed of carbon, aluminium and iron, an observation consistent with the information about the manufacturing process of these particles. (EDX allows elemental analysis and single particle examination is made possible with TEM). At least several tens of particles other than CNT balls, sampled during and prior to the three scenarios, were analysed. These analyses demonstrated that only CNT balls contained the three elements C, Al and Fe and no other. Thus, simultaneous detection of these three elements proved to be a robust signature of the presence of CNT balls. Such signature can be exploited by the LIBS system to detect particles as shown in figure 10.5 for the three scenarios.

The largest particle sampling rate was found for scenario 1 as expected for continuous CNT pouring without ventilation. The spectra recorded during CNT powder handling were examined along with those obtained prior to the handling operations. The simultaneous detection of aluminium, iron and carbon nitride radicals was evidenced during powder handling. The observed carbon nitride radicals originate from the recombination of carbon with nitrogen from the air, when the plasma cools down.

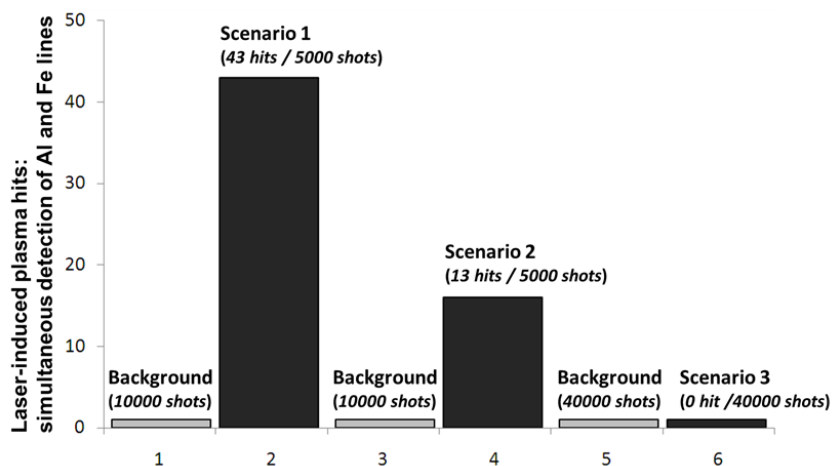


Figure 10.5. CNT detection probability according to the handling scenarios described in section 10.4.2 (Adapted from Ref. 11 with permission from Springer, copyright 2011)

Acting as a marker for carbon detection, CN emission bands were seen more intense in spectra corresponding to CNT powder handling than in those registered prior to handling. The simultaneous detection of the three particle-composing elements was never achieved prior to the handling operations.

All these considerations indicate that the simultaneous detection of aluminium, iron and carbon nitride emission is the signature of a CNT ball being detected within the laser-induced plasma (figure 10.6). These promising results encourage future experiments to make LIBS particle analysis quantitative.

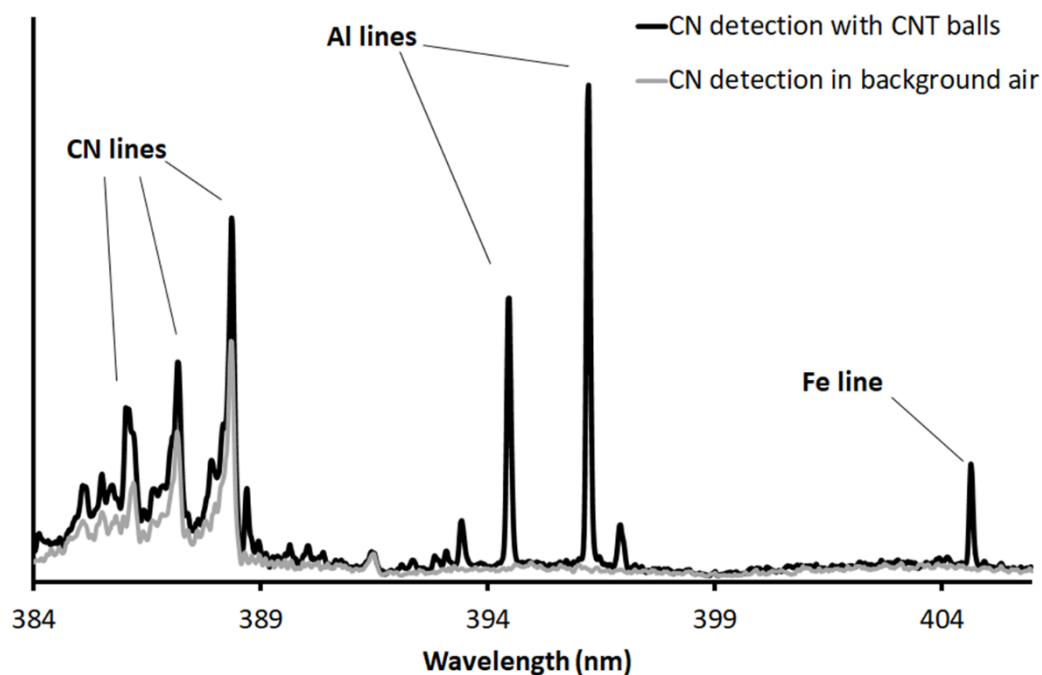


Figure 10.6. Spectral signature of CNT ball detection (Adapted from Ref. 11 with permission from Springer, copyright 2011)

10.5 LIBS detection for process control: example of SiC_x nanopowders

Though the nanoparticle production processes are intended to be reliable, a possible malfunction may occur, and the characteristics of the manufactured powders may differ from the expected values. Among the properties, the chemical composition is of prior importance. So far, its measurement was uniquely performed ex-situ at the end of the manufacturing cycle, after opening the particle collector. Thus, in case of a disruption during the manufacturing process, the composition of the final product differs from the desired composition, and the nanoparticle batch could be lost. This is a real hindrance considering that the cost of such batch is far from being negligible. In this framework, the LIBS technique was seen as a potential candidate for real-time monitoring of the elemental composition of the synthesized product¹⁵.

10.5.1. SiC_x manufacturing

A scheme of the experimental set-up of the laser pyrolysis reactor is presented in figure 10.7. It consists of a reactor equipped with an inlet nozzle at its bottom, an outlet duct at its top and several optical windows for the laser beam passage and the pyrolysis flame monitoring. Reactants, namely SiH₄ and C₂H₂, for SiC_x nanoparticle synthesizes are injected into the pyrolysis reactor through the inlet nozzle with adjustable flow rate. A continuous high-power CO₂ laser beam is expanded to twice its starting diameter with an optical system and focused on the vertical direction using a ZnSe cylindrical lens of 500 mm focal length.

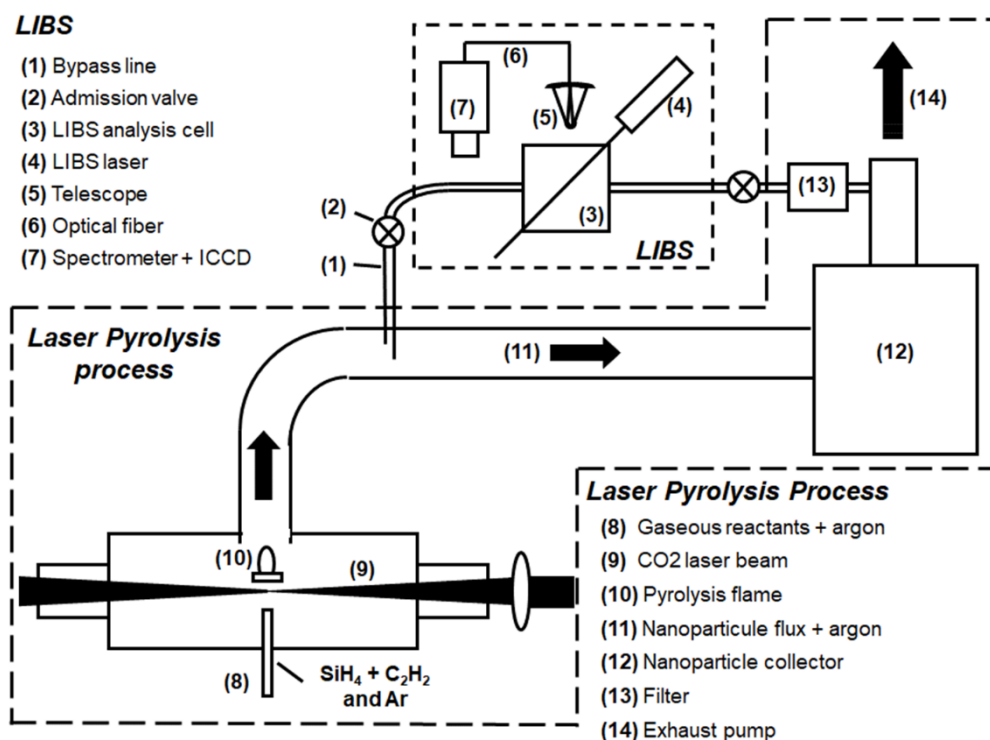


Figure 10.7. Scheme describing the integration of the LIBS system with the pyrolysis reactor.

The resulting beam of 30 mm large elliptical cross-section passes through the reactor perpendicularly to the above-mentioned reactant jet coming out from the nozzle. A wide range of laser power density values for reactant irradiation are accessible by adjusting the distance between the cylindrical lens and the nozzle. The position of maximum focusing corresponds to the maximum irradiance of 50 kW cm^{-2} . A co-flow of argon gas is injected around the reactants in order to confine the reaction. At the same time, a stream of argon sweeps all the inner window surfaces to avoid particle deposition. Eventually, the nanoparticles are evacuated from the reactor with argon as a carrier gas. Then, they are directed towards the nanoparticle collector thanks to a pump placed downstream of the collector and connected to an exhaust-treatment system constituted of a scrubber and a washer. The production rate of this unit can go beyond 1 kg of silicon carbide nanoparticles per hour. The laser pyrolysis reactor setting can be adjusted to produce silicon carbide with various stoichiometries to obtain SiC , SiC_2 , SiC_4 and SiC_8 .

10. 5. 2. LIBS experimental setup

The LIBS apparatus mounted on the laser pyrolysis process is depicted in figures 10.7 and 10.8. In order to carry out the LIBS experiment, a cell through which the nanoparticles flow was installed on the process. A bypass line was designed to achieve a diversion and to enable an on-line continuous sampling from the main stream of nanoparticles.

Using the bypass line, the inlet end of the cell was connected to the nanoparticle production conduit upstream of the nanoparticle collector. The outlet end was linked to the exhaust conduit downstream of the collector. The pre-existent pressure difference between the two connection points sufficed to make the nanoparticles carried by the argon gas stream circulate through the cell for LIBS analysis purposes.

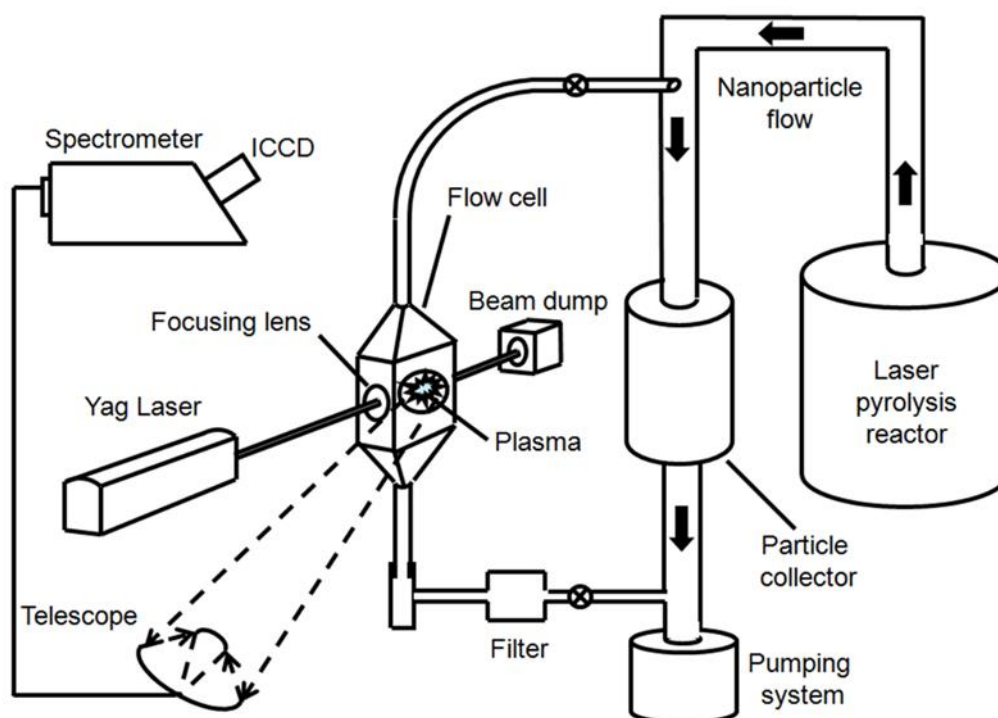


Figure 10.8. LIBS system installed on the laser pyrolysis unit (Adapted from Ref. 3 with permission from Spectroscopy, copyright 2015)

A small filter collector was placed downstream of the cell outlet to prevent the particles from being released in the main line. Nd:YAG laser pulses of 5 ns duration, 50 mJ energy, and 20 Hz repetition rate were focused inside the cell using a fused silica plano-convex lens of 50 mm focal length. The resulting beam waist of about 100 μm led to an estimated laser fluence of 150 J cm^{-2} in the focal plane. The LIBS signal originating from the plasma generated in the argon-nanoparticle mixture was collected through a quartz window perpendicularly to the laser beam with a telescope of 150 mm focal length. The plasma emission was imaged onto the entrance a 50 μm diameter core optical fibre. The fibre was linked to an Echelle spectrometer of 5×10^3 resolving power equipped with a gated CCD camera.

10. 5. 4. Evaluation of SiC_x elemental composition

In appropriate experimental conditions, the laser-induced plasma can be described by the simple model of local thermodynamic equilibrium (LTE) and the plasma emission spectrum can be easily and accurately calculated. The calculation can be further simplified in case of negligible self-absorption, when the photons emitted from the plasma species have insignificant probability of being reabsorbed by the plasma. This case was considered by Ciucci et al.¹⁶ when they firstly proposed compositional analysis via the so-called “calibration-free” LIBS. Thus, instead of comparing the measured spectral line intensities with the intensity of previously recorded calibration curves, the measured intensities are compared to computed spectral line intensities to evaluate directly the elemental composition. Usually, the calculation requires to solve a system of coupled Saha- and Boltzmann equations¹⁷. The problem is significantly reduced in case of moderate ionization, when the neutral atoms dominate the plasma composition. In that case, the fraction ratio S between two elements a and b can be directly derived from the intensities of spectral lines emitted from their atoms $I_{ij}^{a,0}$ and $I_{kl}^{b,0}$ ¹⁵

$$S = \frac{N_{tot}^a}{N_{tot}^b} = \frac{I_{ij}^{a,0} \lambda_{ij}^{a,0} Z^{a,0} g_k A_{kl}^{b,0}}{I_{kl}^{b,0} \lambda_{kl}^{b,0} Z^{b,0} g_i A_{ij}^{a,0}} \times \exp\left(-\frac{E_k^b - E_i^a}{k T}\right). \quad (10.6)$$

Here, λ and A are the wavelength and the transition probability of the transitions, g and E are the statistical weight and the energy of the upper electronic levels, Z is the participation function of neutral atoms, k is the Boltzmann constant. The temperature T is typically deduced from the intensity ratio of spectral lines of the same atom having sufficiently different upper level energies. The carbon over silicon atomic fraction ratio obtained with equation (10.6) for measured intensities of the C I 247.8 nm and Si I 288.1 nm lines is shown in figure 10.9 as a function of the reference fraction ratio. To illustrate the influence of the temperature measurement error on the uncertainty of the deduced fraction ratio, the latter is presented for the maximum and minimum T -values that limit the temperature uncertainty interval.

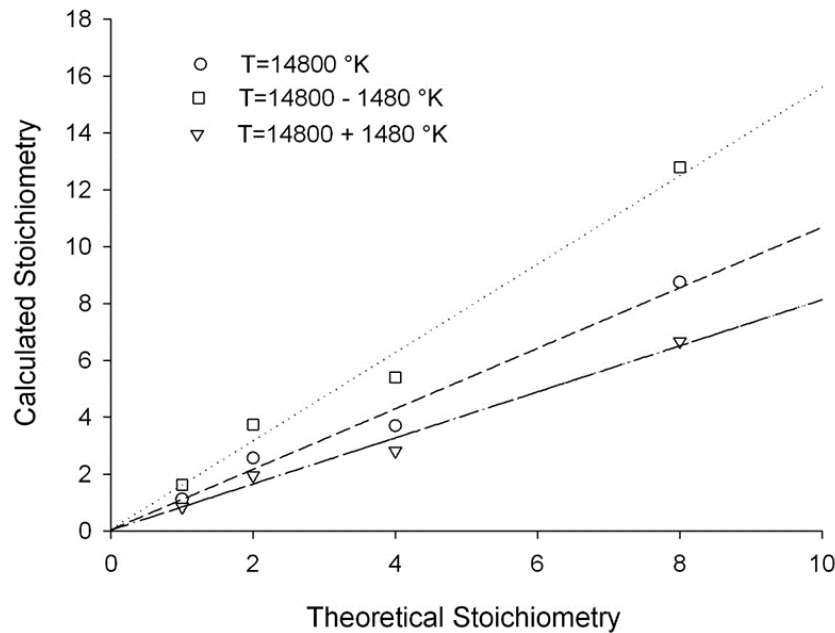


Figure 10.9. Carbon over silicon atomic fraction ratio of SiC_x particles deduced from simplified calibration-free LIBS analysis using equation (10.6). The influence of plasma temperature error on the compositional measurement uncertainty is depicted (Adapted from Ref. 15 with permission from Elsevier, copyright 2008)

The large uncertainty of the compositional measurements of particles shown in figure 10.9 illustrates that accurate calibration-free LIBS analyses are challenging. We therefore summarize in the following section the more general approach of such measurements, and we show that calibration-free LIBS analysis of high analytical performance can be achieved if the appropriate experimental conditions are chosen, and a more sophisticated calibration-free LIBS model is applied.

10.6 Compositional analysis of particles via calibration-free LIBS

10.6.1 Principal and methodology calibration-free LIBS

Compositional analysis via laser-induced breakdown spectroscopy is known to be affected by strong matrix effects that originate from the dependence of the LIBS plasma properties on the composition and the physical properties of the sample⁴. The strong matrix effects render the calibration of the LIBS measurements difficult and lead therefore in many cases to low accuracy of compositional analysis. To overcome these difficulties, calibration-free LIBS analysis has been proposed¹⁶. Based on modelling of the plasma emission spectrum, this approach enables direct analysis via the simple comparison between measured and computed intensities of analytical transitions. The original approach proposed by Ciucci et al. was based on the following hypotheses:

- (i) Sample vaporisation is congruent
- (ii) The plasma is in local thermodynamic equilibrium (LTE)
- (iii) The plasma is spatially uniform
- (iv) Self-absorption of spectral lines is negligible

Although hypotheses (i) and (ii) have been shown to be mostly fulfilled in experimental conditions typical for LIBS experiments, the last two conditions are hardly satisfied. Amended calibration-free LIBS approaches have thus been proposed, most of them were dedicated to the compensation of self-absorption, that was considered to be the main error source of the model-based analytical measurement^{18,19,20}. Most calibration-free approaches were based on the simplified model of a spatially uniform plasma, although gradients of temperature were often evidenced, in particular when LIBS analysis were performed in ambient air²¹. This can be justified for transitions of weak self-absorption by the fact that their emission is dominated by the contribution of the hot plasma core that appears almost uniform^{21,22}.

We can distinguish two types of calibration-free approaches: (i) methods based on the so-called multi-elemental Boltzmann plot^{16,23} and (ii) approaches based on spectra simulation^{24,25,26}. The fundamental physical model behind these two types of approaches is mostly the same: the uniform LTE plasma. The principal difference relies in the way to solve the problem: in the case of the multi-elemental Boltzmann plot, the starting point consist in measuring line-intensities in the measured spectrum, whereas the spectra simulation starts with the spectrum calculation. In both cases, the same parameters have to be retrieved.

Indeed, an n elements composing plasma in LTE is fully described by $n + 1$ parameters that are the temperature T and the number densities of the n elements. For practical purposes, this set of parameters can be replaced by the following equivalent set: the temperature T , the electron density n_e , and the relative fractions C_i of $n - 1$ elements²⁷. If the calibration-free LIBS analysis accounts for self-absorption, an additional parameter intervenes: the plasma size along the line of sight L_p . Thus, $n + 2$ measurements are required involving at least $n + 2$ spectral lines. The relative fractions C_i can be deduced from the intensity measurements of n lines emitted from species of the n elements. The temperature measurement can be performed by measuring for one element the intensity of at least one additional line with a significantly different upper level energy. The electron density can be obtained from Stark broadening of at least one spectral line^{28,29} whereas the plasma diameter can be deduced by observing for one element an additional of significantly different optical thickness³⁰.

The calibration-free LIBS analysis can be operated straightforwardly by performing the measurements successively in an appropriate iteration loop³⁰. Operated in appropriate experimental conditions³¹, such analysis may reach high analytical performance as demonstrated for different types of materials^{32,33}.

10.6.2 Calibration-free LIBS analysis of aerosols in helium

The calibration-free LIBS methodology was rarely applied to compositional analysis of aerosols. This is mainly due to the fact that the model of a spatially uniform equilibrium plasma generally fails as a result of the complex physical processes that occur in the particle-containing breakdown plasma, namely (i) particle heating by the breakdown plasma, (ii) particle vaporisation, and (ii) diffusion of vaporised atoms into the hot gas³⁴. The particles are heated by the breakdown plasma and cooled by vaporization. The vaporized matter in the vicinity of the particles is therefore typically cooler than the breakdown plasma itself. Such temperature gradients are typically expected for breakdown in air or argon, and appropriate modelling is in this case more complex³⁵. The situation is different for breakdown in helium

due to the particular properties of the lightest inert gas. Compared to air and argon, the use of helium leads to two changes that render plasma modelling much simpler: (i) according to the much larger ionization potential of helium, the breakdown plasma temperature is significantly higher, and the particle vaporization is thus faster^{36,37}. (ii) Helium has larger thermal conductivity and the combination of both effects favour rapid vapour-gas thermalisation. Beside the appropriateness for plasma modelling, the use of helium has an additional advantage. For a given temperature, the electron density and those the continuum emission are reduced. The signal-to-noise ratio is therefore enhanced which is of particular interest for the measurements of low-intensity analytical signal originating from the aerosol particles.

10.6.3 Demonstration for Al₂O₃ aerosol analysis via calibration-free LIBS in helium

The compositional analysis of particles via calibration-free LIBS in helium has been demonstrated for aerosols generated from alumina powder with the aid of a vortex mixer³⁸. The experimental setup used for this experiment was similar to that shown in figure 10.4. Here, a larger laser pulse energy of 300 mJ was applied to obtain an irradiance of $1 \times 10^{13} \text{ W cm}^{-2}$ in the focal volume. This ensured highly reproducible breakdown that was almost independent of the presence of particles within the focal volume. The particle size and specific density within the helium flow were measured using an aerodynamic particle size spectrometer to $7.5 \pm 2.5 \mu\text{m}$ and a few mg m^{-3} , respectively. A spectrum recorded with an echelle spectrometer of 5×10^3 resolving power coupled to a gated detector is shown in figure 10.10 for a recording time $t = 1.25 \pm 0.25 \mu\text{s}$ that was found to be most appropriate for the calibration-free LIBS analysis.

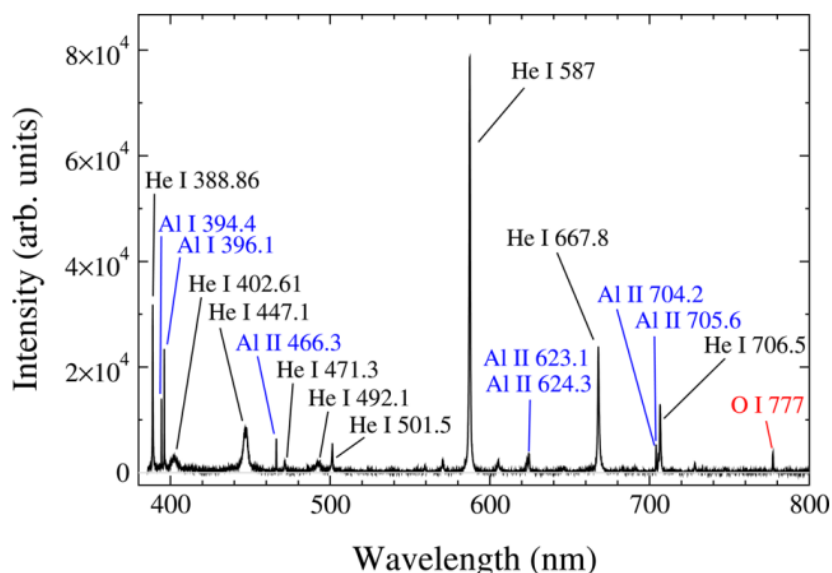


Figure 10.10. Spectrum of the Al₂O₃ particle-containing helium breakdown plasma recorded with a delay of 1.0 μs between the laser pulse and the detector gate. The gate width was set to 0.5 μs (Adapted from Ref. 38 with permission from ACS publications, copyright 2016).

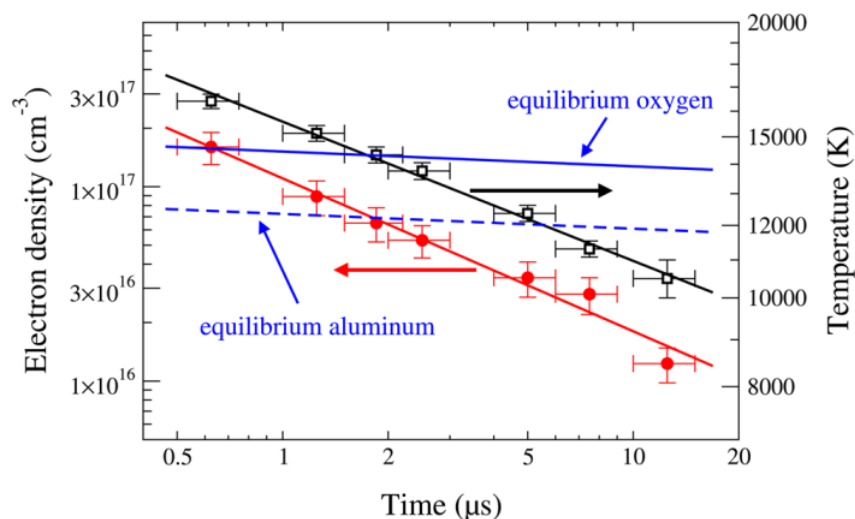


Figure 10.11. Electron density measured via Stark broadening of Al II 704.21 and He I 667.8 nm transitions and temperature deduced from the Saha-Boltzmann plot of aluminium. The minimum electron density required for Boltzmann equilibrium according to the McWhirter criterion is indicated for oxygen and aluminium. (Adapted from Ref. 38 with permission from ACS publications, copyright 2016)

The recording time is chosen as a result of a compromise between large enough signal-to-noise ratio and validity of local thermodynamic equilibrium. In LIBS experiments, the background signal is dominated by the continuum emission due to bremsstrahlung and radiative recombination³⁹. Both effects are associated to the presence of free charges within the plasma that have decreasing number densities as shown in figure 10.11. Accordingly, high signal-to-noise ratio is obtained by using a large recording delay. However, the validity of equilibrium requires a large enough electron density, and the recording delay must thus set short enough (see figure 10.11).

The spectrum recorded for the most appropriate recording delay is displayed in figure 10.12 for the spectral ranges of aluminium neutral atoms (a), aluminium ions (b, c) and oxygen atoms (d) together with the computed spectral radiance. In addition to the lines attributed to the aerosol composing elements, several transitions of the helium buffer gas are observed. As the spectral widths of all measured transitions is accurately reproduced in the computed spectrum, the electron density within the vaporized matter can be assumed to be equal to the n_e -value of the breakdown plasma. This observation supports the hypothesis of a spatially uniform plasma that is expected for aerosol vaporisation by the breakdown plasma generated in helium (see section 10.6.2).

The elemental composition of the aerosols deduced from the calibration-free LIBS measurements is displayed in figure 10.13 for analysis of spectra recorded with different gate delays. It is shown that accurate compositional measurements are possible for measurement times $\leq 1 \mu\text{s}$ only. At larger delays, the equilibrium condition is not any more fulfilled for oxygen (see figure 10.12). This leads to an overpopulation of the upper level of the O I 777 nm transitions, and consequently to an overestimation of the oxygen fraction.

The influence of measurement timing on the accuracy of calibration-free LIBS measurements was also observed in compositional measurements of other oxygen containing materials such as glass³⁰ and sapphire⁴⁰.

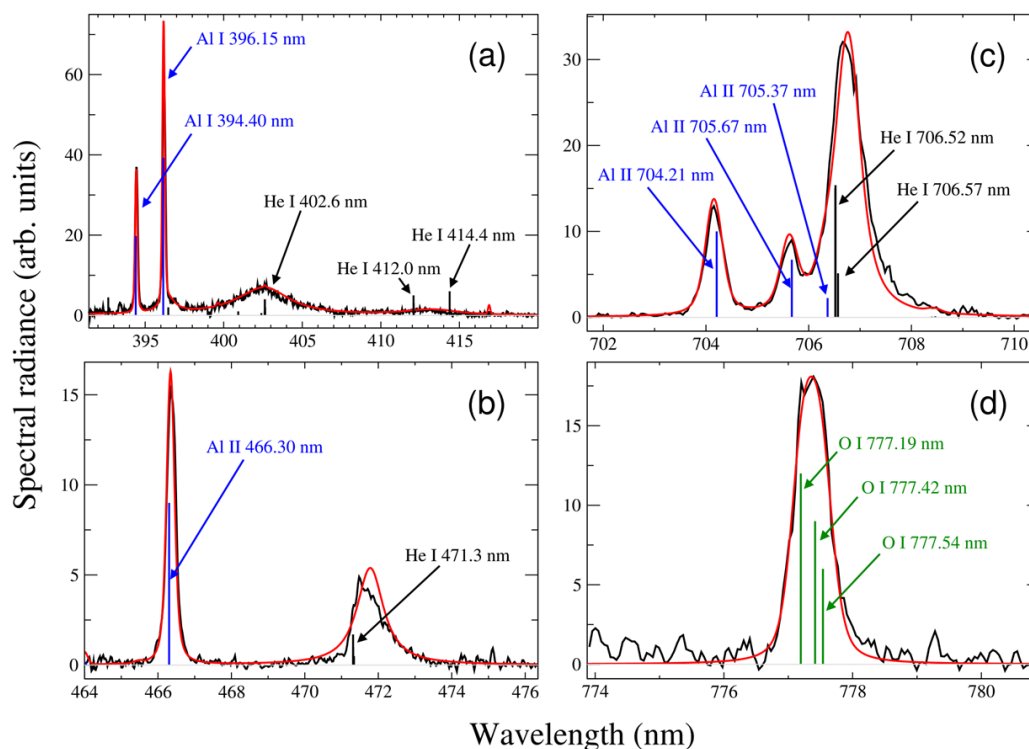


Figure 10.12. Measured (black) and computed (red) spectral radiance for transitions of aluminium, oxygen and helium. The recording time is $t = 1.25 \pm 0.25 \mu\text{s}$. (Adapted from Ref. 38 with permission from ACS publications, copyright 2016)

In summary, calibration-free LIBS can be a powerful tool for analysis, if operated in appropriate experimental conditions. The use of helium favours the formation of a spatially uniform plasma and enables thus robust and accurate modelling of the plasma emission spectrum. In air or argon atmospheres, the temperatures of vaporized matter and the breakdown plasma typically differ, and more complex modelling is required to enable accurate compositional analysis via calibration-free LIBS.

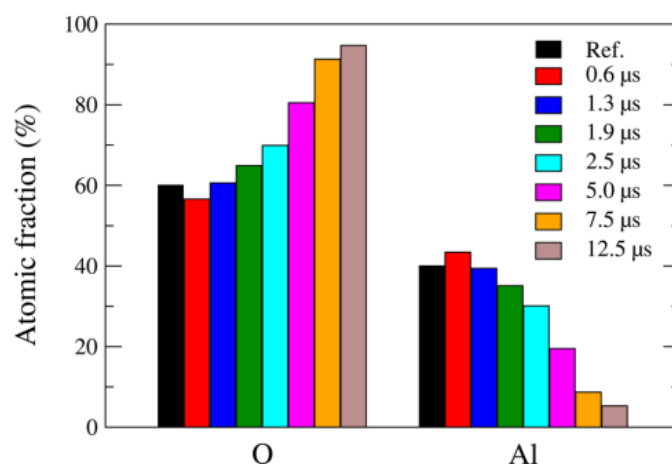


Figure 10.13. Composition of aerosols deduced from the analysis of spectra recorded with different gate delays (coloured bars). The black bars represent the atomic fractions expected for stoichiometric Al_2O_3 . (Adapted from Ref. 38 with permission from ACS publications, copyright 2016)

10.7 Trapping particles in a Radio Frequency (RF) plasma discharge

10.7.1. LIBS coupled with RF plasma: a new way to detect NOAA?

The analysis of particles in a usual cell (like that described in sections 10.4.3 and 10.5.2) or a six-way cross cell raises questions. As emphasized above, the laser-induced plasma has a transient nature, and the laser-induced spark is neither uniform in space nor constant in time. In addition, the laser-induced plasma volume is tiny compared to the inner volume of the LIBS cell. In other words, many particles of the aerosol flow will escape the analysis. This raises the question of particle sampling. A way to sample all collected particles would considerably improve the analysis. A solution may be given by pre-concentrating the particles on a substrate or on a filter. However, analysis based on these solutions were shown to be affected by strong matrix effects⁴¹. Another interesting way to deal with such issue is particle trapping. Such trapping is achieved using a radio frequency plasma discharge. Thus, the LIBS technique and other laser diagnostics may be coupled with the plasma discharge acting as a particle trap. This coupling presents several advantages, and its basic principle is as follows. Particles are injected in the low-pressure RF plasma cell where they remain trapped, frozen in levitation. Particles or nano-objects are therefore accessible to the analysis using laser techniques and even RF plasma diagnostics. Such coupling does present unique features in comparison to current commercially available instruments:

- Particles are trapped within the low-pressure plasma instead of being flowed
- The RF plasma cell makes the particles levitate within the plasma
- The particles are even almost immobilized, frozen
- The RF plasma de-agglomerates agglomerated particles
- The RF cell acts as a pre-concentrator as sampled particles cannot escape the analysis, and remain therefore detectable as long as the RF discharge is on
- Particles may be analysed without using substrates
- Single particle analysis is easily made possible
- Last but not least, elemental composition determination of organic particles may be facilitated using inert buffer gas such as argon or helium

Acting as a pre-concentrator, the coupling of laser spectroscopy diagnostics with the RF discharge brings interesting perspectives for the development of a new “multi-characterization” tool, dedicated to ambient air monitoring and process control, and allowing in the medium run to gain access to the following particle features on-line and in real-time:

- Elemental composition
- Particle size distribution
- Particle morphology
- Particle number density

In this context, experiments were performed to demonstrate the feasibility of particle detection by LIBS within the low-pressure plasma discharge at pressures ranging from 0.25 to 1 mbar.

10. 7. 2. Experimental setup

The particle trap or RF cell presents itself (see figure 10.14) as a 100 mm wide and 100 mm high stainless-steel cell, fitted with four optical windows for particle observation via optical diagnostics. A pair of 60 mm diameter parallel disc-shaped electrodes, separated by a gap of 50 mm, is enclosed within the cell in horizontal position. The electrode located at the bottom is connected to the ground, while the upper electrode is fed by an RF generator that is operated at a frequency of 13.56 MHz. The generator delivers a power of 4 W through a matching network ensuring impedance matching between the generator and the plasma. The RF cell is evacuated using a primary pump down to a pressure of 0.25 mbar. The background gas is then flowed in from the top of the cell using a precision valve. Air was used in these experiments. A Baratron gauge monitored the pressure within the chamber. A particle injector, positioned on the top of the RF cell and described below, was employed to flow in particles into the low-pressure plasma. The RF cell rested upon locknuts screwed on four threaded posts fixed on the experimental bench. Laser probing along a vertical axis was therefore achieved by positioning the locknuts and therefore the RF cell they support at the desired vertical position.

For the time being, injection is assured using a system made up of two components, namely the injector mechanism and a small reservoir containing agglomerated engineered nanoparticle powders. The cylindrical-shaped metallic receptacle of 10 mm diameter and 5 mm height was manually filled in, taking precautions inherent to engineered nanoparticle (ENP) handling.

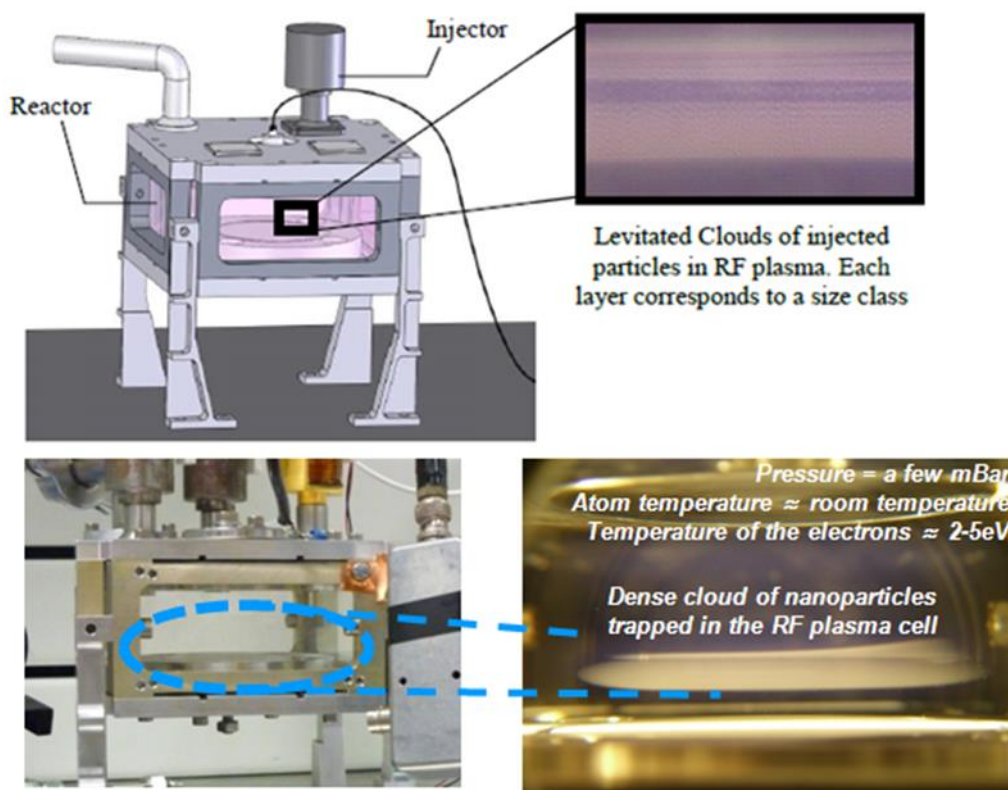


Figure 10.14. Scheme and picture of the RF plasma discharge setup. A cloud of particles levitating between the electrodes can be seen on the picture at the bottom to the right.

Manipulations were conducted in a hood wearing gloves. The receptacle is capped with a 5 μm step mesh grid facing the inner plasma RF discharge chamber when placed in operational position. It was made integral with a metallic rod, part of the injection mechanism. When activated, an electromagnet made the rod and therefore the receptacle move up and down along its axis, thereby exerting a shaking action on the powders, forcing them through the grid right into the plasma discharge. Metal beads of 1 mm diameter laid within the reservoir helped particles passing through the grid.

The LIBS setup (see figure 10.15) is similar to the apparatus described in sections 10.4.3 and 10.5.2, except the difference in the optical path to focus and collect light. Nd:YAG laser pulses of 300 mJ energy and 5 ns duration were applied at a repetition frequency of 20 Hz. The laser beam was expanded to three times the initial beam diameter to reduce the power density incident on the window. A dichroic mirror fully reflective for 1064 nm radiation at 45° incident angle, but otherwise transparent, directed the beam toward a lens of 85 mm focal length used for laser beam focusing. The optical setup makes light collection along the focusing axis possible, given that the dichroic mirror is transparent to the entire spectrum except the laser wavelength. Light emitted by particle disintegration was then collected with the aid of the laser focusing lens and focused with an additional lens of 50 mm focal length on the entrance of an optical fibre of 600 μm core diameter. Optical emission spectra were retrieved from a spectrometer equipped with a gated CCD camera.

Agglomerates of composite nanoparticles of SiC and Al₂O₃ were injected into the RF plasma discharge where they were trapped and remained in levitation. Nanosecond laser pulses were then focused on the trapped particles.

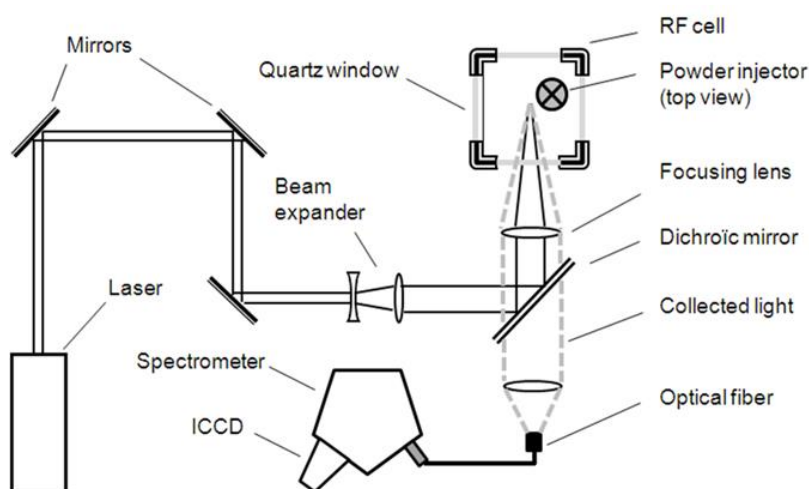


Figure 10.15. Experimental setup of the coupling of the LIBS with a RF plasma discharge (Adapted from Ref 42 with permission from Elsevier, copyright 2013)

10. 7. 3. Summary of the obtained results

The investigations of particle analysis with the radio-frequency plasma confinement led to three main results. First, LIBS detection of particles was achieved via the observation of aluminium and silicon lines with a satisfying signal to noise ratio at the pressure of 0.25 mbar. The sensitivity was high enough to make single particle analysis possible. Spectra corresponding to single particle detection with a unique laser shot are presented in figure 10.16.

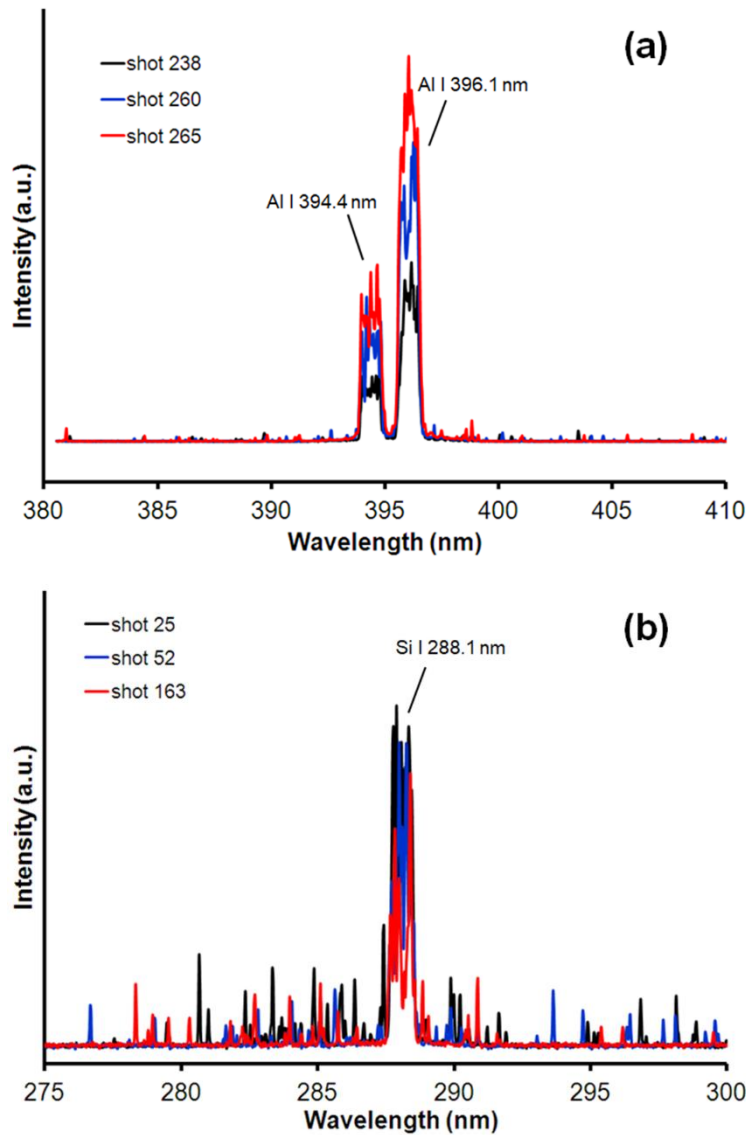


Figure 10.16. Spectra obtained with single shots on (a) Al_2O_3 and (b) SiC_x particles at a pressure of 0.25 mbar (Adapted from Ref. 42 with permission from Elsevier, copyright 2013)

Second, the delay between laser pulse and detector gate for optimized LIBS signal detection was found much shorter than that applied in LIBS particle analysis at atmospheric pressure. Indeed, compared to atmospheric pressure conditions, the microplasma formed on the particles cools much faster at reduced pressure. As a consequence, the plasma temperature corresponding to the maximum LIBS signal is reached much earlier in low-pressure conditions. Thus, the delay for optimized LIBS measurements is much shorter as illustrated by the intensity evolution of spectra shown in figure 10.17.

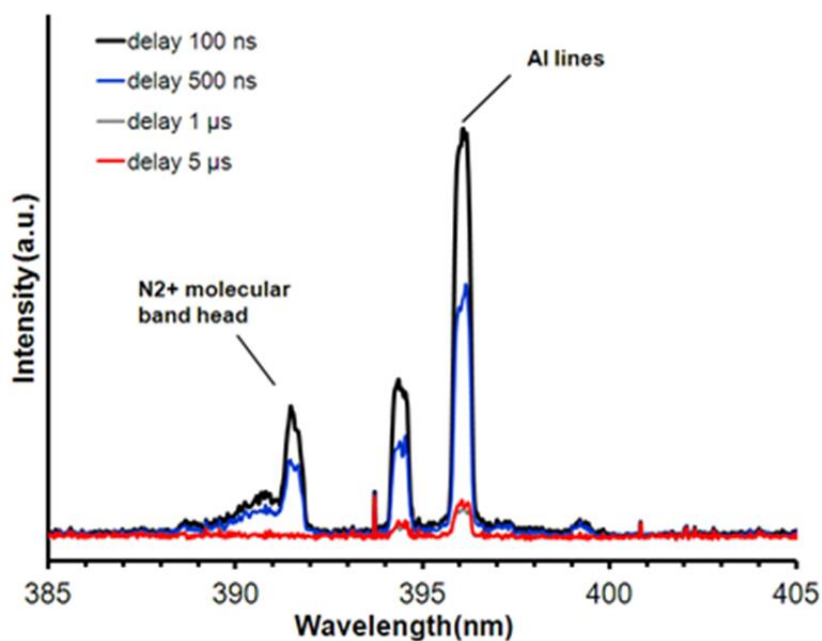


Figure 10.17. Spectra recorded with different delays when probing Al_2O_3 particles within the RF plasma discharge under 0.25 mbar pressure (Adapted from Ref. 42 with permission from Elsevier, copyright 2013)

Third, agglomerates of SiC particles were successfully detected (figure 10.18) at reduced pressure. The obtained results have led to the deposit of a patent that describes the ultrasensitive particle detection method based on LIBS analysis combined with the radio-frequency discharge particle confinement⁴³.

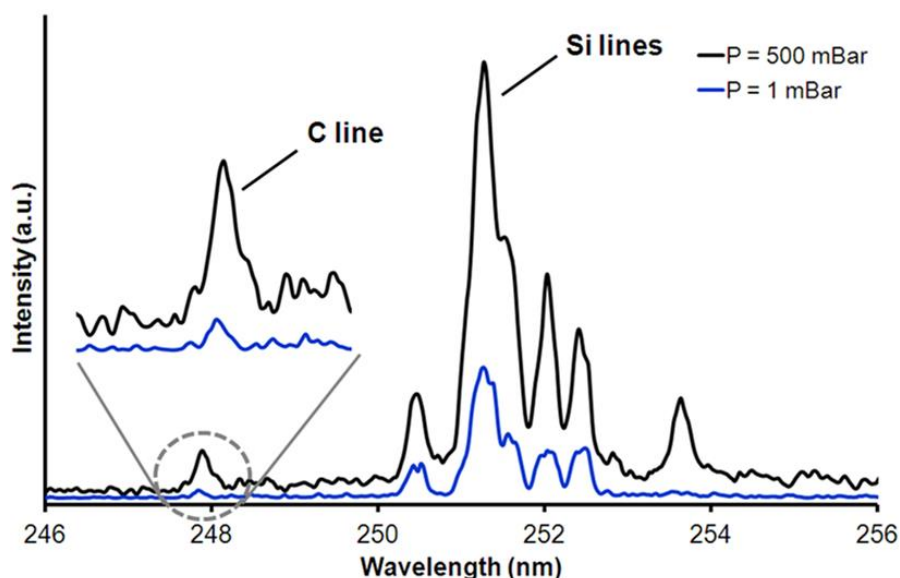


Figure 10.18. Spectra acquired for a single laser shot when probing SiC particles at 500 and 1 mbar. Time delay and integration time were set to 500 ns and 7 μs , respectively. Next to the C I 247.8 nm line can be seen the Si multiplet. The corresponding spectrum is poorly resolved, given the wide entrance slit selected to enhance carbon detection (Adapted from Ref. 42 with permission from Elsevier, copyright 2013).

10.8 Conclusion

The LIBS technique has been successfully applied to detect NOAA for both workplace surveillance and process control. First, the detection of CNT balls was demonstrated by using the reliable spectral signature based on the simultaneous detection of atomic lines from aluminium and iron atoms and emission bands from carbon nitride radicals. These results demonstrated the potentialities of the LIBS technique for CNT ball detection. The next step consisted of quantitative measurements using a proper calibration approach. The experiments made on SiC_x nanopowders demonstrated that LIBS is a potential tool for process control to monitor the chemical composition in real-time. However, the accuracy of such so-called calibration-free LIBS measurements was shown to depend critically on the choice of the experimental conditions and on the sophistication of the computational approach. In particular, it was demonstrated that laser-induced breakdown in helium leads to a spatially uniform plasma that enables accurate compositional measurements of aerosols. In air or argon, the plasma uniformity is typically not reached, and calibration-free LIBS analysis require more complex plasma modelling.

A promising approach of particle detection based on the combination of LIBS analysis with particle trapping in a low-pressure radio frequency plasma was presented. This method was shown to present several advantages. All injected particles are trapped and can potentially be analysed, thereby improving sampling. The analysis is no longer carried out on gas flow where most of the particulates escape the analysis. Organic particle analysis may be made possible without interferences with the C, H, N, O, elements already present in the air when using an inert gas such as argon or helium for RF plasma generation. In addition, the signal-to-noise ratio is enhanced at reduced pressure. The use of other laser diagnostics could be envisaged as well for size and morphology measurements. It is too early to state over the real potentialities of such approach. Further studies are needed to assess these. Eventually, all these examples emphasize the LIBS qualities as a tool to be used in the field outside a usual analytical chemistry laboratory.

References

1. D. W. Hahn and N. Omenetto, *Appl. Spectrosc.*, 2010, **64**, 335A.
2. D. W. Hahn and N. Omenetto, *Appl. Spectrosc.*, 2012, **66**, 347.
3. C. Dutouquet, *Spectroscopy*, 2015, **30**, 24.
4. A. W. Miziolek, I. Schechter, and V. Palleschi, *Laser-Induced Breakdown Spectroscopy: Fundamentals and Applications*, Cambridge University Press, Cambridge, 2006.
5. R. Noll, *Laser-Induced Breakdown Spectroscopy: Fundamentals and Applications*, Springer, Berlin, 2012.
6. D. A. Cremers and L. J. Radziemski, *Handbook of Laser-Induced Breakdown Spectroscopy*, John Wiley & Sons, Ltd, 2013.
7. J. P. Singh and S. N. Thakur, *Laser-Induced Breakdown Spectroscopy*, Elsevier, Second Edition, 2020.
8. D.W. Hahn, W. L. Flower and K. R. Hencken, *Appl. Spectrosc.*, 1997, **51**, 1836.
9. D.W. Hahn and M.M. Lunden, *Aerosol Sci. Technol.*, 2000, **33**, 30.
10. D. Diaz and D. W. Hahn, *Spectrochim. Acta Part B: Atom. Spectrosc.*, 2021, **179**, 106107.
11. B. R'Mili, C. Dutouquet, J.B. Sirven, O. Aguerre-Chariol and E. Fréjafon, *J. of Nanopart. Res.*, 2011, **13**, 563.
12. D. Diaz, D. W. Hahn and U. Panne, in *Laser-Induced Breakdown Spectroscopy*, Ed. J.P. Singh, S. N. Thakur, Elsevier, Second Edition, 2020, Chapter 22, 499-535.

13. F. Danafar, A. Fakhru'l, M. Salleh and D. Biak, *Chem. Eng. J.*, 2009, **155**, 37.
14. T. Amodeo, C. Dutouquet, O. Le-Bihan, M. Attoui and E. Fréjafon, *Spectrochim. Acta Part B: Atom. Spectrosc.*, 2009, **64**, 1141.
15. T. Amodeo, C. Dutouquet, F. Tenegal, B. Guizard, H. Maskrot, O. Le Bihan and E. Frejafon, *Spectrochim. Acta Part B: Atom. Spectrosc.*, 2008, **63**, 1183.
16. A. Ciucci, M. Corsi, V. Palleschi, S. Rastelli, A. Salvetti and E. Tognoni, *Appl. Spectrosc.*, 1999, **53**, 960.
17. H. R. Griem, *Plasma Spectroscopy*, McGraw-Hill, New York, 1964.
18. V. Lazic, R. Barbini, F. Colao, R. Fantoni and A. Palucci, *Spectrochim. Acta Part B: Atom. Spectrosc.*, 2001, **56**, 807.
19. D. Bulajic, M. Corsi, G. Cristoforetti, S. Legnaioli, V. Palleschi, A. Salvetti and E. Tognoni, *Spectrochim. Acta Part B: Atom. Spectrosc.*, 2002, **57**, 339.
20. A.M.E. Sherbini, T.M.E. Sherbini, H. Hegazy, G. Cristoforetti, S. Legnaioli, V. Palleschi, L. Pardini, A. Salvetti and E. Tognoni, *Spectrochim. Acta Part B: Atom. Spectrosc.*, 2005, **60**, 1573.
21. J. Hermann, C. Gerhard, E. Axente and C. Dutouquet, *Spectrochim. Acta Part B: Atom. Spectrosc.*, 2014, **100**, 189.
22. S.V. Shabanov and I.B. Gornushkin, *J. Quant. Spectrosc. Radiat. Transfer*, 2018, **204**, 190.
23. J. A. Aguilera and C. Aragón, *Spectrochim. Acta Part B: Atom. Spectrosc.*, 2007, **62**, 378.
24. J. Hermann, Patent PCT/FR2009/001221, WO 2010/052380 A1, 2009.
25. C. A. D'Angelo, D. M. D. Pace, G. Bertuccelli and D. Bertuccelli, *Spectrochim. Acta Part B: Atom. Spectrosc.*, 2008, **63**, 367.
26. R. Wester and R. Noll, *J. Appl. Phys.*, 2009, **106**, 123302.
27. E. Axente, J. Hermann, G. Socol, L. Mercadier, S. A. Beldjilali, M. Cirisan, C. R. Luculescu, C. Ristoscu, I. N. Mihailescu and V. Craciun, *J. Anal. At. Spectrom.*, 2014, **29**, 553.
28. M. Cirisan, M. Cvejić, M. R. Gavrilović, S. Jovicević, N. Konjević and J. Hermann, *J. Quant. Spectrosc. Radiat. Transfer*, 2014, **133**, 652.
29. M. Burger and J. Hermann, *Spectrochim. Acta Part B: Atom. Spectrosc.*, 2016, **122**, 118.
30. C. Gerhard, J. Hermann, L. Mercadier, L. Loewenthal, E. Axente, C. R. Luculescu, T. Sarnet, M. Sentis and W. Viöl, *Spectrochim. Acta Part B: Atom. Spectrosc.*, 2014, **101**, 32.
31. J. Hermann, D. Grojo, E. Axente, C. Gerhard, M. Burger and V. Craciun, *Phys. Rev. E*, 2017, **96**, 053210.
32. J. Hermann, E. Axente, F. Pelascini and V. Craciun, *Anal. Chem.*, 2019, **91**, 2544.
33. C. Gerhard, A. Taleb, F. Pelascini and J. Hermann, *Appl. Surf. Sci.*, 2021, **537**, 147984.
34. V. Hohreiter and D. W. Hahn, *Anal. Chem.*, 2006, **78**, 1509.
35. P. Dalyander, I. B. Gornushkin and D. W. Hahn, *Spectrochim. Acta Part B: Atom. Spectrosc.*, 2008, **63**, 293.
36. C. A. Henry, P. K. Diwakar and D. W. Hahn, *Spectrochim. Acta Part B: Atom. Spectrosc.*, 2007, **62**, 1390.
37. I. N. Mihailescu and J. Hermann, in *Laser Processing of Materials*, Schaaf, P., Ed. Springer, Berlin, Germany, 2010.
38. M. Boudhib, J. Hermann and C. Dutouquet, *Anal. Chem.*, 2016, **88**, 4029.
39. L. Casanova, S. A. Beldjilali, G. Bilge, B. Sezer, V. Motto-Ros, F. Pelascini, D. Banaru and J. Hermann, *Anal. Chim. Acta*, 2023, to be published.
40. J. Hermann, A. Lorusso, A. Perrone, F. Strafella, C. Dutouquet, and B. Torralba, *Phys. Rev. E*, 2015, **92**, 053103.
41. C. Dutouquet, G. Gallou, O. Le Bihan, J.B. Sirven, A. Dermigny, B. Torralba and E. Frejafon, *TALANTA*, 2014, **127**, 75.
42. C. Dutouquet, G. Wattieaux, L. Meyer, E. Frejafon and L. Bouffendi, *Spectrochim. Acta Part B: Atom. Spectrosc.*, 2013, **83-84**, 14.
43. C. Dutouquet, E. Frejafon, L. Bouffendi, G. Wattieaux and J.P. Dufour, Patent FR 1259101, 2013.